


Stimulated Laser Cooling in a Compact Geometry Using Microfabricated Atomic Beam Collimators

Chao Li^{1,†}, Xiao Chai,¹ Linzhao Zhuo,¹ Bochao Wei¹, Ardalan Lotfi², Farrokh Ayazi,² and Chandra Raman^{1,*}

¹*School of Physics, Georgia Institute of Technology, 837 State Street, Atlanta, Georgia 30332, USA*

²*School of Electrical and Computer Engineering, Georgia Institute of Technology, 777 Atlantic Drive NW, Atlanta, Georgia 30332, USA*

 (Received 25 August 2022; revised 20 August 2023; accepted 29 August 2023; published 19 September 2023)

We have developed a compact and highly efficient assembly for stimulated laser cooling of thermal rubidium atomic beams traveling upon planar silicon devices. Following precollimation via a silicon microchannel array, we perform beam brightening via a blue-detuned optical molasses [Aspect *et al.*, Phys. Rev. Lett. **57**, 1688 (1986)]. Owing to the small size of the chip elements, we require only 8 mW to implement the efficient cooling scheme, making it well suited for future portable atomic sensors that require minimal size, weight, and power consumption. Small mirrors are fabricated and hand-assembled to precisely overlap a strong elliptical standing wave with a sheet-shaped atomic density distribution, with dimensions chosen precisely to match these. We reduce the transverse velocity spread to below 1 m/s within an interaction length of 4.5 mm above the silicon substrate. We use Doppler-sensitive two-photon Raman spectroscopy to characterize the cooling. In contrast to time-of-flight methods utilized previously, this approach requires a much shorter apparatus to achieve similar resolution. This hybrid of passive and active collimation paves the way toward the construction of fully fledged atomic instruments, such as atomic beam clocks and gyroscopes, entirely on-chip through batch-fabricated processes.

DOI: [10.1103/PhysRevApplied.20.034042](https://doi.org/10.1103/PhysRevApplied.20.034042)

I. INTRODUCTION

Atomic instruments such as precision gravimeters [1] and clocks [2] are increasingly making their way to the marketplace. However, current manufacturing methods rely heavily on hand assembly, which drives up cost and lowers yield. Much research effort has been focused on laser-cooled atoms at the chip scale [3], where there is potential for the use of batch fabrication methods that can address some of these challenges. However, the power of automated fabrication has not been fully harnessed for atomic instruments. Existing devices largely rely on the collection of atoms within a three-dimensional (3D) vapor magneto-optical trap (MOT) before they are transferred to the chip. This approach has been the workhorse of laboratory-scale experiments owing to its great flexibility, but it needs to be rethought for practical sensor deployment. For example, small vacuum cells in the millimeter range considerably limit the atom number that can be obtained, and issues remain with achieving high vacuum in

the fabrication process [4]. They also place atomic sensors in a pulsed, rather than a continuous, mode of operation, where there are unwanted dead times that must be accounted for.

Passively collimated atomic beams, with a narrow transverse velocity spread, represent an alternative approach for atomic sensors. These beams have proved useful in many applications, such as atom interferometry [5], guiding [6], and cavity quantum electrodynamics (QED) [7], where the narrow transverse velocity distribution can eliminate Doppler broadening of atomic lines. In addition, vacuum requirements are considerably relaxed in comparison with cold-atom systems [4]. However, passive collimation simply filters the velocity distribution without changing its brightness [8], and therefore greater collimation leads to a loss of signal.

To this end, a combination of passive collimation and transverse laser cooling can substantially increase atomic beam brightness for such experiments [9]. Unfortunately, many of the miniaturization gains from an on-chip architecture are substantially reduced when weak-spontaneous-force laser cooling is used, since this usually requires centimeter distances to take effect. As a result, millimeter MOTs typically contain substantially fewer atoms [10]. By contrast, stimulated forces can be much stronger and

*craman@gatech.edu

†Present address: Research Laboratory of Electronics, Massachusetts Institute of Technology, Cambridge, Massachusetts 02139, USA.

can reduce the slowing distance, although, in free-space experiments, this type of laser cooling has the disadvantage of typically requiring laser power in excess of 100 mW.

In this work, we demonstrate stimulated laser cooling of a thermal rubidium atomic beam on a chip within an operating distance of only 4.5 mm. In contrast to earlier work performed on free-space atomic beams [11], we show that the reduction of volume at the chip scale results in a substantial reduction in laser power to only 8 mW without the need for multipass geometries and/or optical cavities, which could be added in a further step [12,13]. For practical devices, lower power consumption is a key metric, and our results were accomplished using the same physical mechanism for laser cooling as in Ref. [11]. The velocity spread is reduced by about a factor of 5 while still cooling

10^{10} atoms s^{-1} . A key part of the innovation of our work is the geometrical reduction created by the chip geometry and matching of the laser beam to the atomic beam to optimize the power needed while still maintaining practical fluxes. These results pave the way toward on-chip guiding and similar applications needing a higher degree of collimation such as that available from a two-dimensional (2D) MOT.

Our setup, shown in Fig. 1, features small mirrors bonded together with silicon atomic beam collimators [14,15] and a silicon substrate on a copper frame to achieve an overall length of only 8 mm. Starting from a thermal distribution, our atomic beam underwent passive and active collimation as it passed through collimating channels and interacted with cooling lasers. Passive collimation

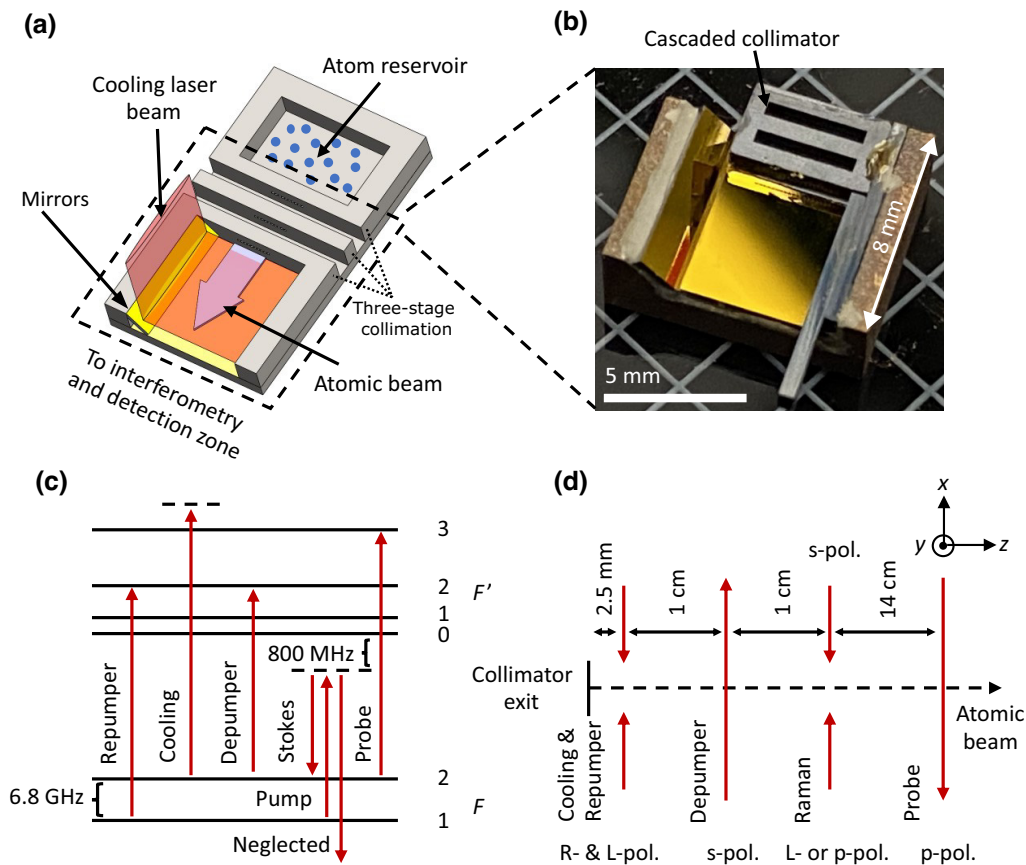


FIG. 1. Overview of the transverse laser cooling experiment and its benchmarking using Doppler-sensitive Raman velocimetry. (a) Conceptualized device containing an atom reservoir, multiple stages of a microcapillary array, and small mirrors. Microchannels direct a continuous stream of atoms to the cooling region with pinpoint accuracy, where the mirrors maneuver laser beams to form a strong standing wave, compressing transverse velocity to the < 1 m/s range within a distance of a few millimeters. (b) Photograph of a manual assembly, containing a microfabricated cascaded collimator made of silicon, alumina-protected gold mirrors, and an electrical-discharge-machined (EDM) copper framework mounting the collimator and laser routing optics. (c) Energy-level diagram of the ^{87}Rb D_2 transitions along with light fields, shown in dark red, used for laser cooling, optical pumping, two-photon Raman transition, and fluorescence measurement. (d) Top view of the experimental configuration, showing the atomic beam (dashed line), going through a sequence of light fields, with their relative spacing marked. Here “R-pol.” and “L-pol.” are right- and left-handed circular polarizations with respect to the direction of propagation; and “s-pol.” and “p-pol.” are linear polarizations perpendicular and parallel (respectively) to the plane of incidence x - O - z .

took place over a distance of 3 mm, followed by active collimation of 4.5 mm, utilizing the entire 8 mm length of the assembled device, as illustrated in Fig. 1(b). We intentionally offset the cooling laser slightly from the collimator exit, leaving a 0.5 mm section without the cooling laser, in order to avoid scattered light. Furthermore, we have thoroughly characterized the cooling using an elegant and compact method based on Doppler-sensitive two-photon Raman spectroscopy. In contrast, conventional atomic beam experiments have employed time-of-flight characterization over meter distances to attain a similar velocity resolution [11,16]. We also present a comparison of our results with those obtained using previous methods.

II. EXPERIMENT

Figure 1(a) presents a future chip-scale atomic beam device that can take full advantage of microelectromechanical systems (MEMS) engineering and vacuum packaging technology [14,17,18]. For example, deep reactive ion etching (DRIE) of silicon can define functional regions for beam formation, ballistic propagation, and interferometry. Wafer bonding can hermetically seal silicon functional and glass capping layers, offering optical access. Using these methods, typical vapor-cell atomic sensors adopt vertical integration in which incident laser beams go through a stack of device layers sandwiching atoms. By contrast, we implemented cooling along an axis within the plane of the wafer to reduce laser power consumption, with the smaller cross-sectional area of the planar atomic beam sheet allowing us to focus more tightly. To direct the laser beam from the top and interact with the atomic beams horizontally, a slanted mirror is necessary. Such a mirror can be realized using a variety of microfabrication protocols [19–22], some of which have found application in making chip-scale pyramidal MOTs [23], vapor-cell clocks [24,25], and NMR gyro [26], but not previously in the context of laser cooling for thermal atomic beams.

In this work, a submillimeter gap between the mirrors and the atomic beam was employed to emulate the architecture of a fully microfabricated and integrated atomic device, as illustrated in Fig. 1(b). This close proximity, however, made the mirrors susceptible to alkali deposition [9]. To address this issue, we implemented cascaded passive collimation and a dielectric protection layer over the gold mirror to guard against alkali attack, as we describe below.

A. The compact collimation assembly

In Fig. 1(b), the silicon collimator is displayed, which has dimensions of 1 mm (height) \times 5 mm (width) \times 3 mm (length). There are 20 thin microcapillaries, each with a square cross section of $100 \times 100 \mu\text{m}^2$. Two 600- μm gaps were machined from the top, halfway through, using a femtosecond laser cutter, partially exposing the

microchannels to free space. The characteristics of these silicon collimators, such as their collimating performance, long-term robustness, and compatibility with different types of atom sources, including pure rubidium and dispenser, have been thoroughly studied in our previous work [14,15,27].

The vertical, bottom, and slanted mirrors have dimensions $1 \times 8 \text{ mm}^2$, $5.5 \times 8 \text{ mm}^2$, and $2 \times 6.5 \text{ mm}^2$, respectively. Here, we briefly summarize the fabrication recipe for making these protected gold mirrors that are resistant to alkali attack. An electron-beam evaporation technique was used to form the mirror coating on a double-side-polished 500- μm -thick silicon substrate. These layers included 20 nm chromium as an adhesive layer, 100 nm gold for increasing reflectivity, and 100 nm alumina (Al_2O_3) as a protective layer [9]. The coated substrate was diced to the desired dimensions, and xenon fluoride gas was used to clean the mirror pieces by removing silicon particles generated during the dicing step.

All components were manually glued to an EDM copper framework using vacuum-compatible epoxies (EPO-TEK 353ND and Master Bond Supreme 18TC). Unfortunately, the edges of the vertical mirror were damaged during the gluing process, and therefore a replacement mirror was overlaid on top of the damaged mirror [it appears as the extruded piece in Fig. 1(b)]. In addition, an extra piece of thin silicon with approximate dimensions $8 \times 14 \text{ mm}^2$ was mounted vertically, immediately above the third stage of the cascaded collimator (not shown). This extra piece was to prevent off-axis atomic vapor from entering the atomic beam region downstream, as in our previous work [14,15]. The laser cooling assembly, including the copper framework, has a total volume of $\sim 0.25 \text{ cm}^3$. The silicon collimator and mirrors occupy about only half of it. This miniature assembly was then attached to a conventional rubidium oven, as in our previous work [14,15]. A detailed description of a compact oven design for atomic beam production is given in Appendix D.

B. Stimulated laser cooling

Figure 1(c) shows the energy-level diagram that we relied on to perform the stimulated laser cooling within the compact assembly. Here, we used two separate diode laser systems (DLC DL PRO 780 S) for the repumper and the cooling beams, respectively. The repumper was on-resonance with the $F = 1$ to $F' = 2$ transition. The stimulated transverse cooling beam was blue-detuned from the $F = 2$ to $F' = 3$ transition by $\delta_c/2\pi$ MHz, where $\delta_c/2\pi$ could be tuned in the range from 40 to 95 MHz, corresponding to the range from 6.6Γ to 16Γ , where $\Gamma = 2\pi \times 6 \text{ MHz}$ is the natural linewidth of the ^{87}Rb D_2 transition. By assigning a red detuning of these values, the sign of the stimulated forces could be flipped, causing heating of the atoms.

Using a tapered amplifier (MOGLabs MOA003), we were able to provide enough power to create an intense standing wave for the stimulated transverse cooling over the range of laser powers used in this work. A separate repumper was merged with the cooling beam using a fiber polarization combiner (Thorlabs PFC780A). We set the cooling beam output to σ^+ to achieve optimized laser cooling for the stretched states $|F = 2, m_F = 2\rangle$ and $|F = 3, m_F = 3\rangle$. For the laser cooling process, the intense light field was sufficient to clearly define the quantization axis along $+\hat{x}$ for m_F . For example, 1 mW of laser power averaged over the small cooling beam size led to a Rabi frequency of 6Γ , which was much larger than the Larmor frequency of ^{87}Rb , which is submegahertz under the Earth's magnetic field.

C. Raman velocimetry and its resolution

Figure 1(d) illustrates the light fields through which atomic beams sequentially passed after leaving the collimation assembly. Table I summarizes their beam sizes and optical powers. The passive collimation and active laser cooling took 8 mm of the propagation distance in total. Preparing atomic states with the depumper, performing the Raman velocimetry, and probing the fluorescence took another 16 cm. Consequently, the fluorescence of the $F = 2$ state was detected downstream on a dark background, without interference from scattered light of other laser beams.

We used a distributed Bragg reflector laser (Photodigm Mercury TOSA DBR), red-detuned by 800 MHz from the $F = 1$ to $F' = 0$ transition as shown in Fig. 1(c), to generate the pump frequency. This carrier then passed through a fiber-coupled electro-optic modulator (EOM; PM-0K5-10-PFA-PFA-780), with a fed-in microwave power (from a Windfreak SynthHD PRO v2) of 10.6 dBm and frequency near $\omega_{\text{HFS}}/2\pi$, which is the hyperfine splitting of the $F = 1, 2$ ground states. We set the EOM power to produce roughly equal zeroth- and first-order sidebands, which were used as the pump and Stokes beams for the

Doppler-insensitive spectroscopy. We scanned their difference frequency via the microwave source, with the step time and step frequency set as 1 ms and 0.02 MHz. Therefore, it took the microwave source 5 s to fully sweep ± 50 MHz over the hyperfine resonance.

In Fig. 2(a), the pump and Stokes fields coherently and adiabatically transferred atoms from $|F = 1\rangle$ to $|F = 2\rangle$ via the stimulated Raman transition. We used co-propagating circularly polarized beams for Doppler-insensitive transitions and counter-propagating lin \perp lin beams for Doppler-sensitive ones. To achieve the latter, we sent an extra portion of the DBR laser power from the opposite direction with respect to the EOM component, as explained above.

1. Doppler-insensitive case

We measured the Doppler-insensitive Raman transition under weak excitation without canceling the Earth's magnetic field and other stray fields. The atomic beam traveled along $+\hat{z}$, roughly pointing to 32°NE in the laboratory with geographic coordinates (33°N , 84°W). Therefore, the k -vectors of the Raman beams were not aligned to the direction of the Earth's magnetic field, and all three projected σ^+ , σ^- , and π components were present after decomposition with respect to a quantization axis defined by the direction of the Earth's field. Each Raman beam could thus drive all allowed one-photon transitions ruled by $\Delta m_F = -1, 0, 1$ [28,29]. There were then nine possible types of transitions in total, given by two photons labeled with an arbitrary pair of polarization states, i.e., π - π , π - $\sigma^{+/-}$, $\sigma^{+/-}$ - π , σ^+ - $\sigma^{+/-}$, and σ^- - $\sigma^{+/-}$. The Zeeman shifts associated with those transitions were equal to $(m_F + m'_F) \times 0.70 \text{ MHz/G} \times B$, considering an overall change in the magnetic quantum number following $\Delta m_F^o = m'_F - m_F = 0, \pm 1, \pm 2$, with the ± 2 transitions being neglected owing to their much smaller transition strengths.

Figure 2(b) displays the measured Doppler-insensitive Raman spectra zoomed into the ± 2 MHz range from a full sweep of ± 50 MHz as we scanned the microwave source. Except for the two-photon transitions mediated by σ^+ - σ^- and σ^- - σ^+ polarizations, all other aforementioned transitions should be visible, resulting in seven peaks in the data [28]. We fitted these peaks to seven Gaussians (see Appendix A) and determined that the peak centers exhibit a linear Zeeman shift, as shown in Fig. 2(c), with a slope corresponding to $B = 0.31$ G. The linewidths are transit-time-limited and approximately 0.3 MHz, but they are more complex because peaks overlap at this magnetic field level. Therefore, we allowed the width to be a fitting parameter.

2. Doppler-sensitive case

We performed Doppler-sensitive Raman velocimetry at higher laser power (see Table I) to (i) enhance the signal-to-noise ratio and (ii) enable the Raman process

TABLE I. Diameters and powers of laser beams in Fig. 1.

Laser beam	$2w_z$ (mm) ^a	$2w_y$ (mm) ^a	Power (mW)
Repumper	4.5	0.21	6–8
Cooling	4.5	0.21	3.0–61
Depumper	2.0	2.0	8
Raman Stokes	1.0	1.0	0.3
Raman pump (co) ^b	1.0	1.0	0.3
Raman pump (ct) ^c	0.8	0.8	2.0
Probe	5.8	5.8	5–7

^a w_y and w_z are the $1/e^2$ Gaussian beam waists.

^bCo-propagating component for Doppler-insensitive cases.

^cCounter-propagating component for Doppler-sensitive cases.

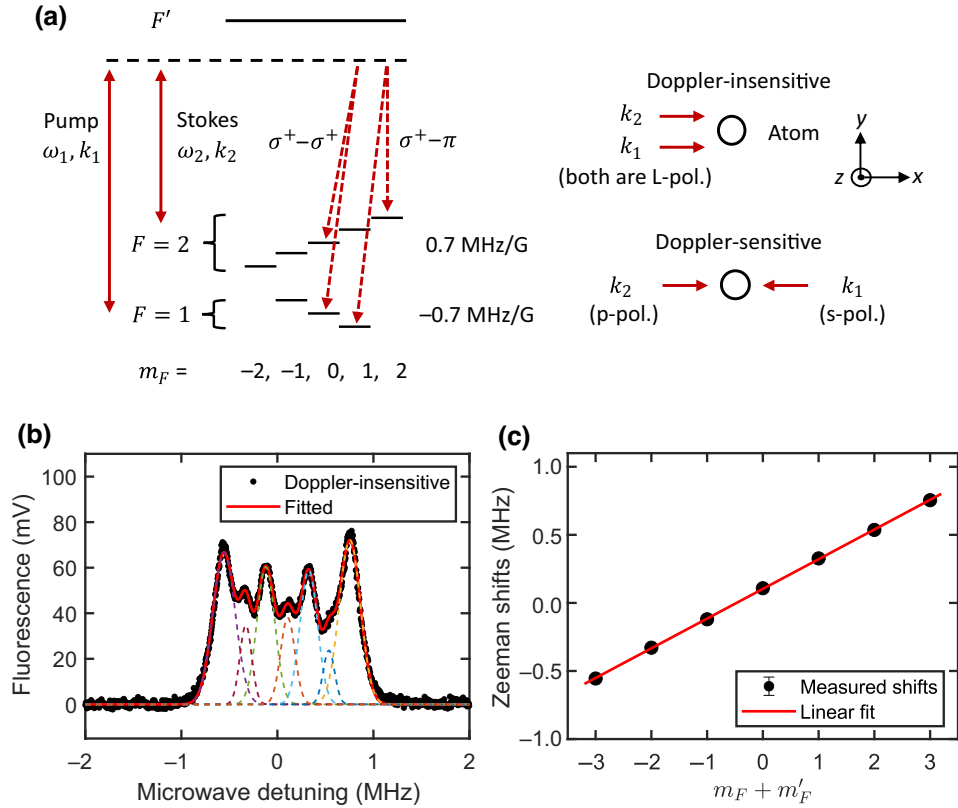


FIG. 2. Working principle of Raman velocimetry. (a) Relevant energy levels of the ^{87}Rb D_2 transition along with co-propagating (counter-propagating) light fields driving the Doppler-insensitive (Doppler-sensitive) Raman transition. Shown in the left-hand part are two representative transitions with $\Delta m_F^o = 0$ or 1, which is the overall change of m_F after a two-photon transition. Here, polarization states are defined with respect to a quantization axis along the Earth field (see text for discussion). (b) Measured Doppler-insensitive Raman spectra containing transit-time, power, and Zeeman broadening. (c) Zeeman shifts extracted for magnetic sublevels: $m_F + m'_F = 0$ and ± 2 are for $\Delta m_F^o = 0$ transitions; and $m_F + m'_F = \pm 1$ and ± 3 are for $\Delta m_F^o = \pm 1$ transitions. Details on the spectral fitting are provided in Appendix A.

on a faster time scale compared with Larmor precession. This allows us to discuss the Raman process with respect to a quantization axis along the propagation direction of the Raman beam. For this configuration, the Raman process transferred atoms pre-depumped in the $F = 1$ state back to $F = 2$ for those satisfying $\delta_r = 2k v_x$ within the narrow linewidth of the Raman transition, where δ_r is the two-photon detuning. The effective Rabi frequency governing such a coherent population transfer from $|F = 1\rangle$ to $|F = 2\rangle$ is simply proportional to $\sum (E_p \langle F = 1, m_F | d | F', m_{F'} \rangle E_s \langle F = 2, m_F | d | F', m_{F'} \rangle)$, counting all allowed transitions, where E_p and E_s are the pump and Stokes electric fields, and $\langle F, m_F | d | F', m_{F'} \rangle$ are their associated transition dipole matrix elements between the ground state $|F, m_F\rangle$ and the excited state $|F', m_{F'}\rangle$ [30].

We then decompose the pump and Stokes fields into circular polarization bases, according to $\hat{z} = (1/\sqrt{2})(-\hat{e}_+ + \hat{e}_-)$ and $\hat{y} = (i/\sqrt{2})(\hat{e}_+ + \hat{e}_-)$, where \hat{e}_+ (\hat{e}_-) drives the σ_+ (σ_-) transition. Our Doppler-sensitive laser setup comprises two counter-propagating laser beams. One of

the beams is polarized along z , with only the Raman pump frequency component. The other beam is polarized along y and EOM modulated to have both the Raman Stokes and pump frequency components. Because of quantum destructive interference, the co-propagating Raman pair can only weakly drive the Raman transition, while the counter-propagating Raman pair has much larger effective Rabi frequency. Therefore, the effect of the zeroth EOM sideband is ignored and this configuration is effectively Doppler-sensitive.

III. RESULTS

Hot-wire ionizing or fluorescence imaging techniques deduce the span of transverse velocities from the spatial spread of atoms [11,16,31]. Assuming all atoms emerge from a source with negligible size and an atom is probed in the far field at location z , its transverse velocity can be estimated according to $v_x = vx/z$, where x is the offset of an atom from the central axis, and v is the longitudinal velocity. Therefore, these techniques cannot be applied to

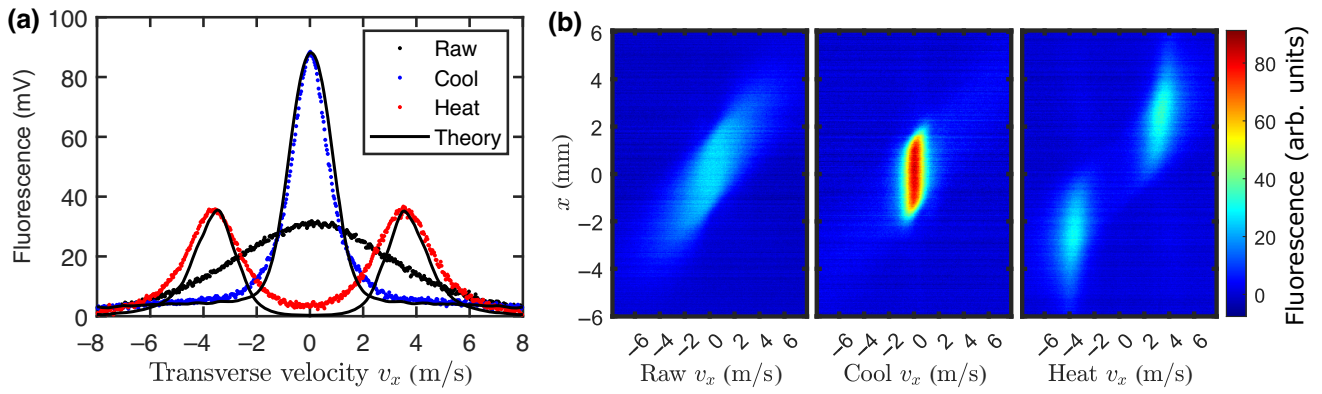


FIG. 3. Raman velocimetry for thermal atomic beams perturbed by an intense laser standing wave. (a) Measured fluorescence versus two-photon detuning $\delta_r = 2kv_x$ of the Doppler-sensitive Raman transition, where k is the wave vector of the ^{87}Rb D_2 transition and v_x is the transverse velocity of the atoms. Black dots (HWHM = 3.6 ± 0.3 m/s) are for the cooling beam off; blue dots (HWHM = 0.84 ± 0.03 m/s) are for the cooling beam on with positive detuning ($\delta_c/2\pi = +40$ MHz); and red dots are for the cooling beam on with negative detuning ($\delta_c/2\pi = -40$ MHz). The curves are theoretical predictions given by the Fokker-Planck equation. (b) A hyperspectral analysis allows us to obtain separate spatial and spectral information as δ_r is scanned (see Appendix B).

a dense array of atomic beams with a few millimeter width, especially when the beam propagation distance is limited within approximately a centimeter, as in chip-scale atomic beam devices [18]. In contrast to probing the atoms spatially, two-photon Raman velocimetry can directly resolve the transverse velocity in the frequency domain, where the transit-time broadening, given the finite size of laser beams driving the Raman transition, sets the limit on Doppler resolution.

Figure 3 shows our principal data. An incident power of only 7.8 mW creates an intense standing wave with a maximum Rabi frequency of 72Γ under laser detunings of $\pm 6.6\Gamma$, comparable to that of Ref. [11]. In Fig. 3(a), we plot the measured fluorescence versus the microwave detuning under three scenarios. All data sets presented here and in the rest of the paper have subtracted background measured at $v_x = 20$ m/s. The raw spectrum shows an original transverse velocity distribution without perturbation by the laser standing wave. The measured HWHM of ~ 4 m/s is in very good agreement with our previous results for an identical cascaded collimator that was characterized via a Doppler-sensitive one-photon cycling transition [14]. In our previous study, artifacts already appeared in the wings of the deconvolved velocity distribution because the intrinsic power-broadened natural linewidth contributed significantly to the measured spectral width. In this work, as seen in Fig. 2(b), the two-photon Raman transition exhibits an HWHM linewidth of less than 1 MHz, which is significantly smaller than the two-photon Doppler HWHM of our atomic beams, approximately 9 MHz. As a result, a deconvolution to retrieve the transverse velocity distribution is not required for the quick comparison presented here.

The cooled spectrum demonstrates that the width of the velocity distribution immediately reduces by a factor of

4.3 once the laser cooling is activated. The best-cooled result with the minimum HWHM, as displayed later in Fig. 4(c), rounds this factor to 5. The ratio of the measured cooled and raw spectra at near-zero v_x indicates that the brightness of the atomic beam has been enhanced by a factor of 3. The heated spectrum reveals that the sign of the stimulated forces has been reversed, and atoms are pushed toward the shoulder protruding around ± 3.5 m/s. In addition, we conducted fluorescence imaging to retrieve the spatial distribution of Raman-selected atoms and to further verify the brightness enhancement. The hyperspectral plots in Fig. 3(b) show that the cooled atom beams, originating from 20 channels, roughly preserve their original size of 3 mm [14], even after a total propagation distance of more than 16 cm.

The theoretically predicted fluorescence in Fig. 3(a) is calculated by solving the following Fokker-Planck equation (see, e.g., Refs. [32–35]):

$$\frac{\partial p}{\partial t} = -\frac{1}{m} \frac{\partial}{\partial v_x} (Fp) + \frac{1}{m^2} \frac{\partial^2}{\partial v_x^2} (Dp),$$

where $p(v_x, t)$ is the transverse velocity distribution, m is the atomic mass, and $F(v_x)$ and $D(v_x)$ are velocity-dependent force and diffusion coefficients, respectively. Given the Rabi frequency Ω and detuning Δ , $F(v_x)$ and $D(v_x)$ are evaluated using a continued-fraction method [32,36]. For simplicity, we ignore the spatial dependence of the laser-beam intensity and approximate the Rabi frequency as its average value $\Omega = 36\Gamma$ [36]. The evolution time is 12 μs , as given by $t_e = 2w_z/\bar{v}_B$, where $2w_z = 4.5$ mm is the beam diameter and $\bar{v}_B = 372$ m/s is the atomic beam mean velocity along the longitudinal direction given a nozzle temperature of 135 °C [37]. The initial

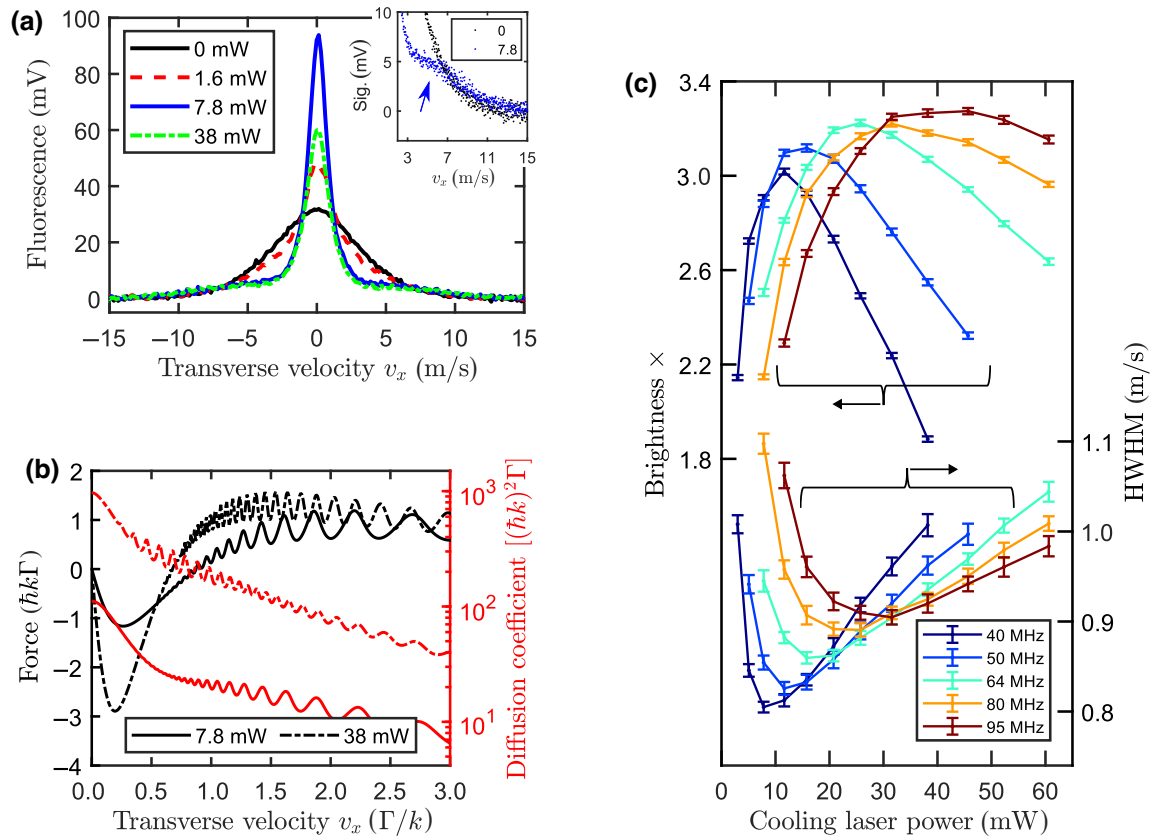


FIG. 4. Power and detuning dependence of laser cooling. (a) Fluorescence signal versus power, showing the progression of laser cooling. The inset zooms into the velocity tail of the raw and best-cooled spectra. (b) Corresponding dipole forces and diffusion coefficients computed for the best-cooled and overshoot cases in panel (a). In panels (a) and (b), $\delta_c/2\pi = +40$ MHz. Solid lines are for lower power and dashed lines are for higher power. The force (diffusion) profile is an odd (even) function, and so the negative-velocity region is not shown. (c) Brightness gain and the corresponding spectral width extracted from data like those shown in panel (a) at different blue detunings as the laser power is scanned across a broad range. The upper (lower) group of curves refers to the axis on the left (right).

condition is deconvolved from the raw experimental data in Fig. 3(a).

We compare our experiment with a previous free-space experiment on Cs thermal atomic beams [11]. The previous experiment required more than 10 cm to achieve a combination of passive and active collimation, which consumed 70 mW of laser power. Our experiment has successfully achieved a similar protocol on a subcentimeter chip-scale platform consuming nine times less laser power. In addition, microfabricated collimators and mirrors are flush against each other during manual assembly. This naturally enables precise alignment between the atomic beam and the laser standing wave in the cooling zone. Alignment uncertainty is measured to be $< 1^\circ$ under an optical microscope after we glue the collimator and mirrors together. Any significant misalignment would be manifested as an asymmetry between two shoulder peaks [11] given a spectral measurement like that in Fig. 3(a), supposing that perfect orthogonality is achieved for all other intersections between laser and atom beams. In the third

panel of Fig. 3(b), we note the existence of a slight asymmetry in fluorescence intensity for atoms at $\sim \pm 4$ m/s. This is mainly attributable to the imperfect orthogonality between the probe laser beam and the atomic beam for this particular data set.

Another unique advantage results from the one-dimensional (1D) nature of an atomic beam array and the precision match between the laser mode and the vertical size of the atomic beams close to the collimator exit. The laser cooling power required typically increases as an atomic beam gets larger. However, power consumption can stay constant as we pack more channels into this 1D microcapillary array, within the Rayleigh range for a given laser-beam size, because one laser standing wave cools them all. Compared with spatial probing methods, our Raman velocimetry diagnostic method does not require a propagation distance of meters, which was previously essential, to reveal the divergence angle of a well-collimated atomic beam. In principle, all experimental state preparation, Raman velocimetry, and detection

sequences could be conducted within another subcentimeter propagation distance after the laser cooling stage, with careful management of the scattered light. This is indispensable for benchmarking the performance of future fully integrated chip-scale atomic beam devices, considering the limited transit length on a chip.

In the following, we use Raman velocimetry to study the dependence of laser cooling on laser intensity and detuning and compare the data with theoretical predictions.

Figure 4(a) shows the progression of cooling versus incident power. As the laser power goes up from 1.6 to 7.8 mW, stimulated forces become larger, shortening the transverse velocity damping time from 30 to 5 μ s. We estimate these numbers by computing the slope of the force profile close to zero transverse velocity. At 1.6 mW, the evolution time $t_e = 12 \mu$ s is not enough to accomplish the cooling process given a damping time of 30 μ s, leading to the incomplete cooling shown as a dashed curve in Fig. 4(a). At 7.8 mW the cooling is nearly complete. However, one can distinguish fine details of the force profile from the wings of the spectrum. The inset in Fig. 4(a) reveals a knee near 5 m/s. This is near the region where the force flips its sign close to Γ/k , and agrees with the theoretical force profile shown in Fig. 4(b), where the solid black curve crosses zero force also at $\sim \Gamma/k$, defining the capture range for transverse velocities. The measured spectra at 38 mW also suggest that excessive laser power at a fixed detuning can cause the transverse temperature to increase due to larger dipole force fluctuations at a higher light intensity.

In addition to results at a blue detuning of 40 MHz, we replicate the same velocimetry measurement at $\delta_c/2\pi = 50, 64, 80,$ and 95 MHz. Results are shown in Fig. 4(c). This convenient approach allows us to determine a minimum HWHM and a maximum brightness enhancement at each detuning as we scan the cooling power across a broad range. Furthermore, increasing both detuning and power in a coordinated manner can further enhance the maximum brightness gain. We attribute this to a larger velocity capture range accumulating and cooling more atoms toward zero v_x according to computed force profiles at larger detunings and higher intensities. An example of a force profile at a Rabi frequency of 1000Γ and a detuning of 200Γ can be found in Ref. [38].

To better understand the coordination between the cooling power and detuning, we also repeat our theoretical machinery, as developed for Fig. 4(b), and the results are shown in Fig. 5. The blue and red dots correspond to the power and detuning settings that result in the highest brightness gain and the smallest HWHM, respectively, as shown in Fig. 4(c). The stepping sequences are labeled as 1 to 5, as we increase the detuning from 40 to 95 MHz. These results clearly indicate that we are moving toward a region with a larger force and capture range, consistent with the observed increase in brightness enhancement.

The slightly larger diffusion coefficient also explains the broader HWHM.

Both the knee shown in Fig. 4(a) and the capture range shown in Fig. 5 indicate that the cascaded collimator is too good for the passive collimation stage and there is not much left for the stimulated cooling to do due to atom depletion. Cascaded filtering by the silicon collimator leaves very few atoms beyond ± 5 m/s range according to Fig. 4(a). Therefore, if we assume an ordinary collimator is used [14], with an HWHM ≈ 8 m/s that still fits well

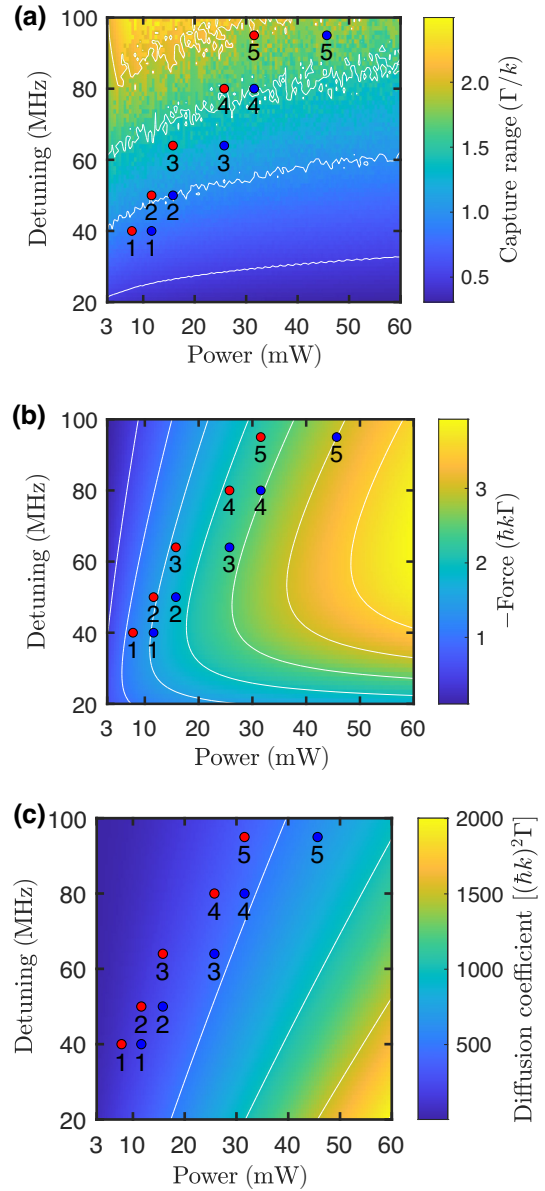


FIG. 5. Numerical calculations of (a) the capture range, (b) the maximum force magnitude, and (c) the diffusion coefficient at zero v_x computed for a broad range of detunings and laser powers. White lines serve as contours to guide the eye as experimental parameters sweep across the contour lines. See the text for further discussion on dots.

within our capture range, we estimate it can lead to another factor-of-5 improvement in the absolute beam brightness, given the peak value and the spectral width reported in our previous work [14].

IV. DISCUSSION

Several immediate extensions can further improve the laser cooling performance. For instance, multipass 2D transverse laser cooling using blue-detuned standing waves has been investigated in recent literature, particularly for molecular beams [39,40]. More than 50 reflections have been demonstrated to recycle optical power and extend the interaction length between Rb atomic beams and the cooling zone [9]. However, this has not been studied in the context of stimulated forces on a chip scale. By implementing these approaches, as well as other multipass reflective structures [41], we can further enhance the efficiency of 2D collimation on this chip-scale atomic beam platform in future works.

An increased interaction length to avoid the $1/e^2$ Gaussian tail truncation (see Table I) and optimized cooling laser-beam profile can facilitate atom channeling and even adiabatic cooling [42], reducing the transverse atomic momentum rms value to nearly the recoil limit [16,33]. Our current work did not optimize the laser standing wave's intensity spatial profile, but it can be adaptively controlled using a spatial light modulator [43,44], as opposed to previous studies that relied on a Gaussian tail [16,33]. The recoil-limited transverse divergence angle is estimated to be $v_r/\bar{v}_B = 16 \mu\text{rad}$, with $v_r = 5.9 \text{ mm/s}$ [30]. For comparison, our Raman transition linewidth yields a divergence angle resolution of 1.6 mrad, limited by the Zeeman and transit-time broadening. Therefore, we also need to improve the velocimetry resolution correspondingly in future work. According to this resolution, we detail our estimation on the achieved atomic beam brightness value of $4.1 \times 10^{13} \text{ atoms s}^{-1} \text{ sr}^{-1}$ in Appendix C. This value could potentially increase by two orders of magnitude if all measured atoms within the 1.6-mrad resolution window were cooled to the recoil limit. Additionally, this work did not optimize the geometry of the passive collimation stage. By employing a combination of Monte Carlo simulations and laser cooling simulations [14,45,46], the collimating channel geometry can be further optimized while considering the laser cooling capture range.

For future devices targeting practical applications, a long lifetime, low power consumption, and high beam brightness are all desired. However, using longer collimators can potentially lead to atom-atom collisions inside microcapillaries, which may broaden the transverse velocity distribution [47]. Additionally, a longer collimator does not improve atomic beam brightness [8], as it acts as a passive filter for a cosine emitter, similar to an orifice. Moreover, high oven temperatures consume power

and rubidium more rapidly, reducing the longevity of the on-chip source.

The reduction of the transverse velocity span by a factor of 5 can allow one to guide atoms using 25 times lower current with on-chip wires [48–50]. Limited current capacity for on-chip wires also favors guiding laser-cooled atoms. It is important to note that 1D collimation is already useful for many applications. For instance, a chip-scale Raman-interrogated atom interferometer gyroscope does not require laser cooling along the vertical dimension if the vertical size of the Raman interrogation beam is larger than the atomic beam size within a centimeter-scale propagation distance. Using an ^{87}Rb -enriched source and optical pumping techniques to prepare all atoms into the $m_F = 0$ state can effectively enhance the atomic beam brightness as well [51–53].

In summary, we have demonstrated stimulated laser cooling on a chip, reducing atomic transverse speeds to 80 cm s^{-1} within a small, subcentimeter geometry that includes both the atomic beam collimator and cooling region. Only 8 mW were needed, substantially lower than the tens of milliwatts typically used in larger geometries typical of free-space cooling. Our results point to multiple possibilities for on-chip atom manipulation, including beam brightening for Raman interferometry and atom guiding. These could open up new avenues for atomic inertial sensing on-chip.

ACKNOWLEDGMENTS

C.L. acknowledges Alexandra Crawford for reading and commenting on the manuscript, and Anosh Daruwalla and Benoit Hamelin for providing earlier test samples. C.L. thanks Martin Zwierlein for useful course materials and discussions.

C.L. and C.R. conceived the experiments; C.L. designed the assemblies, conducted the experiments, and analyzed the data, with experimental assistance from X.C., L.Z., and B.W.; X.C. and C.L. performed theoretical calculations; A.L. fabricated the small silicon mirrors; C.L. wrote the manuscript, with input from A.L., X.C., and C.R.; C.R. and F.A. supervised the study.

APPENDIX A: SPECTRAL FITTING

References [28,29] have systematically studied Raman resonances in the presence of magnetic fields, taking into account all Zeeman sublevels for cold rubidium atoms. Accordingly, we fit the experimentally measured spectra in Fig. 2(b) to a summation of seven Gaussian peaks, $f(x) = \sum_{i=1}^7 a_i \exp[-((x - b_i)/c_i)^2]$. For each Gaussian peak, the HWHM is $\sqrt{\ln(2)} c_i$. We then manually constrain $a_i \in [0, 100]$ and $b_i \in [-1, 1]$, as evident from the spectra. The upper bound for c_i , or $\text{HWHM}/\sqrt{\ln(2)}$, can be deduced from the distinct separation of multiple peaks in Fig. 2(b), where the difference $b_7 - b_1$ is approximately

TABLE II. Fitted Gaussian coefficients with uncertainties for Fig. 2(b).

i	a_i (mV)	b_i (MHz)	c_i (MHz)	$m_F \rightarrow m'_F$
1	66.7 ± 0.6	-0.555 ± 0.003	0.165 ± 0.003	$-1, -2$
2	34.7 ± 2.5	-0.329 ± 0.005	0.088 ± 0.006	$-1, -1;$
3	60.3 ± 0.7	-0.120 ± 0.004	0.132 ± 0.011	$0, -1; -1, 0$
4	38.0 ± 2.9	0.108 ± 0.006	0.106 ± 0.013	$0, 0$
5	58.8 ± 0.8	0.327 ± 0.004	0.129 ± 0.011	$1, 0; 0, 1$
6	23.6 ± 2.2	0.536 ± 0.006	0.085 ± 0.009	$1, 1$
7	72.1 ± 0.6	0.754 ± 0.002	0.156 ± 0.003	$1, 2$

1.3 MHz. This observation implies that the HWHM has an upper bound of $(b_7 - b_1)/6$, leading to the constraint $c_i \in [0, 0.26]$. Here, we summarize all the fitted coefficients along with their uncertainties in Table II. In the text, we used the expression $0.4\bar{v}_B/w_z$ to estimate the transit-time broadening [54].

APPENDIX B: FLUORESCENCE DETECTION

The fluorescence spectra and images shown in Figs. 2–4 were collected using a set of 2-in. lenses positioned 9 cm above the probe region, resulting in a collection efficiency of about 1.3%. The output of the photodiode (Thorlabs DET100A2 with a responsivity of 0.6 A W^{-1}) was converted to voltage by a current amplifier (DL Instruments 1211) with a gain setting of 10^9 V A^{-1} and a claimed minimum rise time of 0.25 ms.

Accounting for the transit time through the probe region, which is approximately $16 \mu\text{s}$ given the longitudinal beam mean velocity \bar{v}_B , the probe laser-beam size, and the resonant photon scattering rate, we estimated a coefficient of $1.1 \times 10^{10} \text{ atoms s}^{-1} \text{ V}^{-1}$ for converting the measured fluorescence voltage to atomic flow. This coefficient is specific to ^{87}Rb atoms in the $F = 2$ state. The uncertainty is about 24% considering errors in determining the transit time and the conversion of fluorescence power to photocurrent. Data acquisition was performed using an oscilloscope with a 10 kS s^{-1} sampling rate at 12-bit resolution (PicoScope 5242D). To achieve better comparisons in scenarios such as the one shown in Fig. 3(a), we averaged 40 neighboring data points.

We also determined the correlation between the transverse velocity distribution and the spatial spread of the atomic beam in the probe region by directly replacing the photodiode with a camera featuring $2464 (x) \times 2056 (z)$ pixels and a unit-cell size of $3.45 \mu\text{m}$ (Imaging Source DMK 33UX264). The imaging system had a magnification of $M = 0.7$, which was used to convert the images of atoms to their spatial locations. However, the fluorescence imaging method operated more slowly than the photocurrent detection method because the exposure time was set to be 1/10 s or 1/15 s to provide sufficient sensitivity.

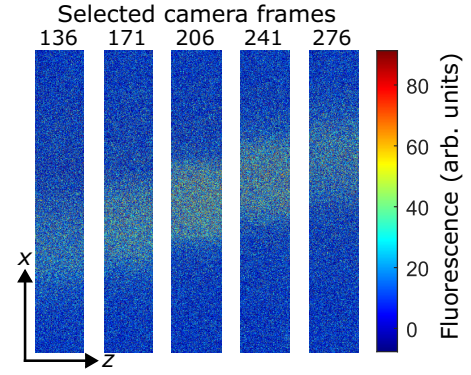


FIG. 6. Camera footage processing. Fluorescence images after background subtraction show atoms in the $F = 2$ state. The Doppler-sensitive two-photon Raman transition selects their transverse velocity v_x . No laser cooling is in action for this data set, corresponding to the “Raw” case shown in Fig. 3(b). There are $2464 (x) \times 400 (z)$ pixels for the region of interest of each frame. Their frame indices as shown correspond to $v_x = -2.7, -1.3, 0, 1.3, \text{ and } 2.7 \text{ m s}^{-1}$. The coordinate system maps onto Fig. 1.

The former setting was used for recording raw and heated spectra, and the latter for the laser-cooled case.

We accordingly reduced the microwave-source linear scan range to $\pm 20 \text{ MHz}$ for fine velocity resolution. Over this range, we collected 401 frames for the “cool” case and 411 frames for the “raw” and “heat” cases, with the center frame corresponding to zero two-photon detuning. To illustrate this, we display five frames, numbered 136, \dots , 276, in Fig. 6, highlighting atoms with relatively small v_x . For each frame, we averaged the beam image over the z direction, which results in a distribution of atom density versus x at a specific two-photon detuning corresponding to the frame index. We then repeated this protocol for different v_x values to generate a hyperspectral plot that shows atom distributions against both spatial position and transverse velocity, as presented in Fig. 3(b).

APPENDIX C: ESTIMATION OF ATOMIC BEAM BRIGHTNESS

We estimated the atomic beam brightness based on the peak fluorescence voltage shown in Fig. 4(a). Using the voltage-to-flow conversion coefficient from Appendix B, 94 mV corresponds to $1.0 \times 10^9 \text{ atoms s}^{-1}$ for ^{87}Rb atoms in the $F = 2$ state. However, due to the thermal longitudinal speed distribution, only approximately 50% of all ^{87}Rb atoms are transferred from the $F = 1$ state, as prepared by the depumper illustrated in Fig. 1(d).

The divergence angle along the y dimension is approximately 31 mrad , resulting from the diameter $2w_y = 0.8 \text{ mm}$ of the Raman beam and the Raman-beam-to-source distance of 25.5 mm . Along the x dimension, the divergence angle is about 1.6 mrad , given the Doppler

selectivity $\text{HWHM} \lambda$ divided by \bar{v}_B [see Sec. II C 2 and Fig. 2(b)]. The two divergence angles encompass a solid angle of 5.1×10^{-5} sr.

Considering the atomic flow emitted within this finite solid angle, we estimate an averaged atomic beam brightness of 4.1×10^{13} atoms s^{-1} sr^{-1} for all ^{87}Rb atoms. This value already takes into account the factor of 2 associated with the thermal average of Raman Rabi population transfer and includes all 20 collimating channels. However, it does not consider ^{85}Rb , as the active collimation stage does not influence it.

We estimate the brightness uncertainty to be approximately 35%. This value includes both the calibration error of the atomic flow rate (as described in Appendix B) and the uncertainty in the Raman population transfer fraction. The latter can be easily determined by measuring the $F = 1$ fluorescence in the probe region in future work. Additionally, we note that the on-axis atomic beam brightness is about 1.4 times larger than the averaged brightness value due to the relatively large vertical geometrical angle or solid angle used. This factor can be obtained by assuming that the probability density distribution for v_y follows a triangular shape with an HWHM of 13 mrad, as previously reported for a cascaded collimator [14]. Therefore, the average brightness value can be regarded as a lower bound for the on-axis atomic beam brightness.

APPENDIX D: ATOMIC BEAM OVEN DESIGN

A 101 copper tube, with an outer diameter of 3/8 in. and length of 4 in., serves as the main body of the oven and passes through a ring-shaped Ultem PEI spacer glued at the center of a bored blank KF40 flange. This spacer thermally isolates the oven body from the supporting flange. Another short, pinched-off copper tube containing a glass ampoule of 200 mg rubidium is attached to the *ex vacuo* end using an in-line Swagelok tube union. The capsule section can be replaced when all the rubidium is depleted. On the *in vacuo* end, there is a customized copper holder of diameter 5/8 in. with a rectangular opening at its center to accommodate and mate with the laser cooling assembly.

This nozzle head is glued to the oven body with a 1 cm quartz tube in between, serving as another critical thermal break. This transparent quartz neck also offers access to measure the atomic vapor pressure inside the oven from absorption. The customized copper holder is externally threaded. A dual set of fine-gauge insulated wires is wrapped into the threaded grooves. One set of resistive wires is made of nichrome, while the other conductive set is composed of copper, with currents running in opposite directions with respect to the helical direction. Without generating any bias magnetic fields, running dc through them maintains the nozzle head at a higher temperature than the oven body, thus preventing rubidium from clogging the silicon collimator.

The KF flange surrounding the oven body contains double-pore ceramic electrical feedthroughs, which supply current to the resistive coil wrapped on the nozzle head and read the nozzle and neck temperatures with two 10 k Ω glass bead thermistors. All joints are glued together using vacuum-compatible epoxies as mentioned in the text, with the caution that Master Bond Supreme 18TC is applied to regions requiring good thermal conductivity. Finally, the entire oven is attached to a 6 \times 6 \times 6 in.³ vacuum chamber, and the encapsulated rubidium ampoule can be cracked by compressing the copper tube once the vacuum pressure reaches $\sim 10^{-5}$ Torr. About half of the copper tube oven is outside the vacuum chamber and is heated by a rope heater. A proportional-integral-derivative (PID) controller and a thermocouple are used to keep the oven body temperature at 110 $^\circ\text{C}$. Temperature differences across the entire copper oven are < 15 $^\circ\text{C}$. A current of 0.16 A is needed to maintain the nozzle head at 135 $^\circ\text{C}$, consuming approximately an additional 1 W of electrical power.

-
- [1] V. M noret, P. Vermeulen, N. Le Moigne, S. Bonvalot, P. Bouyer, A. Landragin, and B. Desruelle, Gravity measurements below $10^{-9}g$ with a transportable absolute quantum gravimeter, *Sci. Rep.* **8**, 1 (2018).
 - [2] S. Knappe, V. Shah, P. D. Schwindt, L. Hollberg, J. Kitching, L.-A. Liew, and J. Moreland, A microfabricated atomic clock, *Appl. Phys. Lett.* **85**, 1460 (2004).
 - [3] M. Keil, O. Amit, S. Zhou, D. Groswasser, Y. Japha, and R. Folman, Fifteen years of cold matter on the atom chip: Promise, realizations, and prospects, *J. Mod. Opt.* **63**, 1840 (2016).
 - [4] J. McGilligan, K. Gallacher, P. Griffin, D. Paul, A. Arnold, and E. Riis, Micro-fabricated components for cold atom sensors, *Rev. Sci. Instrum.* **93**, 091101 (2022).
 - [5] P. R. Berman, *Atom Interferometry* (Academic press, 1997).
 - [6] T. Takekoshi and R. Knize, Optical Guiding of Atoms Through a Hollow-Core Photonic Band-Gap Fiber, *Phys. Rev. Lett.* **98**, 210404 (2007).
 - [7] R. Thompson, G. Rempe, and H. Kimble, Observation of Normal-Mode Splitting for an Atom in an Optical Cavity, *Phys. Rev. Lett.* **68**, 1132 (1992).
 - [8] J. Giordmaine and T. Wang, Molecular beam formation by long parallel tubes, *J. Appl. Phys.* **31**, 463 (1960).
 - [9] C. Slowe, L. Vernac, and L. V. Hau, High flux source of cold rubidium atoms, *Rev. Sci. Instrum.* **76**, 103101 (2005).
 - [10] A. Isichenko, N. Chauhan, D. Bose, J. Wang, P. D. Kunz, and D. J. Blumenthal, Photonic integrated beam delivery for a rubidium 3D magneto-optical trap, *Nat. Commun.* **14**, 3080 (2023).
 - [11] A. Aspect, J. Dalibard, A. Heidmann, C. Salomon, and C. Cohen-Tannoudji, Cooling Atoms with Stimulated Emission, *Phys. Rev. Lett.* **57**, 1688 (1986).
 - [12] C. E. Tanner, B. P. Masterson, and C. E. Wieman, Atomic beam collimation using a laser diode with a self-locking power-buildup cavity, *Opt. Lett.* **13**, 357 (1988).

- [13] M. Hoogerland, J. Driessen, E. Vredenburg, H. Megens, M. Schuwer, H. Beijerinck, and K. Van Leeuwen, Bright thermal atomic beams by laser cooling: A 1400-fold gain in beam flux, *Appl. Phys. B* **62**, 323 (1996).
- [14] C. Li, X. Chai, B. Wei, J. Yang, A. Daruwalla, F. Ayazi, and C. Raman, Cascaded collimator for atomic beams traveling in planar silicon devices, *Nat. Commun.* **10**, 1 (2019).
- [15] C. Li, B. Wei, X. Chai, J. Yang, A. Daruwalla, F. Ayazi, and C. Raman, *et al.*, Robust characterization of microfabricated atomic beams on a six-month time scale, *Phys. Rev. Res.* **2**, 023239 (2020).
- [16] J. Chen, J. G. Story, J. J. Tollett, and R. G. Hulet, Adiabatic Cooling of Atoms by an Intense Standing Wave, *Phys. Rev. Lett.* **69**, 1344 (1992).
- [17] J. Kitching, Chip-scale atomic devices, *Appl. Phys. Rev.* **5**, 031302 (2018).
- [18] G. D. Martinez, C. Li, A. Staron, J. Kitching, C. Raman, and W. R. McGehee, A chip-scale atomic beam clock, *Nat. Commun.* **14**, 3501 (2023).
- [19] M.-S. Ahn, J. Jeon, K.-W. Jang, and K.-H. Jeong, Large-area and ultrathin MEMS mirror using silicon micro rim, *Micromachines* **12**, 754 (2021).
- [20] K. P. Rola, K. Ptasinski, A. Zakrzewski, and I. Zobel, Silicon 45° micromirrors fabricated by etching in alkaline solutions with organic additives, *Microsyst. Technol.* **20**, 221 (2014).
- [21] A. Brockmeier, F. S. Rodriguez, M. Harrison, and U. Hilleringmann, Surface tension and its role for vertical wet etching of silicon, *J. Micromech. Microeng.* **22**, 125012 (2012).
- [22] R. Chutani, N. Passilly, J. Albero, M. Baranski, and C. Gorecki, Deep wet-etched silicon cavities for micro-optical sensors: Influence of masking on 111 sidewalls surface quality, *J. Microelectromech. Syst.* **23**, 585 (2014).
- [23] M. Trupke, F. Ramirez-Martinez, E. Curtis, J. Ashmore, S. Eriksson, E. A. Hinds, Z. Moktadir, C. Gollasch, M. Kraft, and G. Vijaya Prakash, *et al.*, Pyramidal micromirrors for microsystems and atom chips, *Appl. Phys. Lett.* **88**, 071116 (2006).
- [24] H. Nishino, M. Hara, Y. Yano, M. Toda, Y. Kanamori, M. Kajita, T. Ido, and T. Ono, A reflection-type vapor cell using anisotropic etching of silicon for micro atomic clocks, *Appl. Phys. Express* **12**, 072012 (2019).
- [25] R. Chutani, V. Maurice, N. Passilly, C. Gorecki, R. Boudot, M. Abdel Hafiz, P. Abbé, S. Galliou, J.-Y. Rauch, and E. De Clercq, Laser light routing in an elongated micromachined vapor cell with diffraction gratings for atomic clock applications, *Sci. Rep.* **5**, 1 (2015).
- [26] R. M. Noor, V. Gundeti, and A. M. Shkel, in *2017 IEEE International Symposium on Inertial Sensors and Systems (INERTIAL)* (IEEE, 2017), p. 156.
- [27] B. Wei, A. Crawford, Y. Andeweg, L. Zhuo, C. Li, and C. Raman, Collimated versatile atomic beam source with alkali dispensers, *Appl. Phys. Lett.* **120**, 144001 (2022).
- [28] S. DeSavage, J. Davis, and F. Narducci, Controlling Raman resonances with magnetic fields, *J. Mod. Opt.* **60**, 95 (2013).
- [29] S. DeSavage, K. Gordon, E. Clifton, J. Davis, and F. Narducci, Raman resonances in arbitrary magnetic fields, *J. Mod. Opt.* **58**, 2028 (2011).
- [30] D. A. Steck, Rubidium 87 D line data, URL <http://steck.us/alkalidata> (2021).
- [31] D. Mitra, N. B. Vilas, C. Hallas, L. Anderegg, B. L. Augenbraun, L. Baum, C. Miller, S. Raval, and J. M. Doyle, Direct laser cooling of a symmetric top molecule, *Science* **369**, 1366 (2020).
- [32] K. Berg-Sorenson, Y. Castin, E. Bonderup, and K. Molmer, Momentum diffusion of atoms moving in laser fields, *J. Phys. B: At., Mol. Opt. Phys.* **25**, 4195 (1992).
- [33] J. Chen, J. G. Story, and R. G. Hulet, Evolution of atomic motion in an intense standing wave, *Phys. Rev. A* **47**, 2128 (1993).
- [34] M. Drewsen and N. Vitanov, Intensifying atomic beams by two-step transverse laser cooling, *J. Phys. B: At., Mol. Opt. Phys.* **26**, 4109 (1993).
- [35] K. Molmer, The optimum Fokker-Planck equation for laser cooling, *J. Phys. B: At., Mol. Opt. Phys.* **27**, 1889 (1994).
- [36] V. Minogin and O. Serimaa, Resonant light pressure forces in a strong standing laser wave, *Opt. Commun.* **30**, 373 (1979).
- [37] N. Ramsey, *Molecular Beams* (Oxford University Press, New York, 1985).
- [38] J. Dalibard and C. Cohen-Tannoudji, Dressed-atom approach to atomic motion in laser light: The dipole force revisited, *JOSA B* **2**, 1707 (1985).
- [39] I. Kozyryev, L. Baum, K. Matsuda, B. L. Augenbraun, L. Anderegg, A. P. Sedlack, and J. M. Doyle, Sisyphus Laser Cooling of a Polyatomic Molecule, *Phys. Rev. Lett.* **118**, 173201 (2017).
- [40] X. Alauze, J. Lim, M. Trigatzis, S. Swarbrick, F. Collings, N. Fitch, B. Sauer, and M. Tarbutt, An ultracold molecular beam for testing fundamental physics, *Quantum Sci. Technol.* **6**, 044005 (2021).
- [41] X. Liu, Ph.D. thesis, State University of New York at Stony Brook (2022).
- [42] S. Li, M. Zhou, and X. Xu, Analysis of atomic beam collimation by laser cooling, *Sci. Rep.* **8**, 9971 (2018).
- [43] W. Williams and M. Saffman, Two-dimensional atomic lithography by submicrometer focusing of atomic beams, *JOSA B* **23**, 1161 (2006).
- [44] X. He, P. Xu, J. Wang, and M. Zhan, High efficient loading of two atoms into a microscopic optical trap by dynamically reshaping the trap with a spatial light modulator, *Opt. Express* **18**, 13586 (2010).
- [45] R. Kersevan and M. Ady, *et al.*, in *10th International Particle Accelerator Conference*, Vol. 6 (2019).
- [46] S. Eckel, D. S. Barker, E. B. Norrgard, and J. Scherschligt, PyLCP: A Python package for computing laser cooling physics, *Comput. Phys. Commun.* **270**, 108166 (2022).
- [47] H. Beijerinck and N. Verster, Velocity distribution and angular distribution of molecular beams from multichannel arrays, *J. Appl. Phys.* **46**, 2083 (1975).
- [48] N. Dekker, C. Lee, V. Lorent, J. Thywissen, S. Smith, M. Drndić, R. Westervelt, and M. Prentiss, Guiding Neutral Atoms on a Chip, *Phys. Rev. Lett.* **84**, 1124 (2000).
- [49] R. Folman, P. Krüger, D. Cassettari, B. Hessmo, T. Maier, and J. Schmiedmayer, Controlling Cold Atoms Using Nanofabricated Surfaces: Atom Chips, *Phys. Rev. Lett.* **84**, 4749 (2000).

- [50] J. Sauer, M. Barrett, and M. Chapman, Storage Ring for Neutral Atoms, *Phys. Rev. Lett.* **87**, 270401 (2001).
- [51] P. Tremblay and C. Jacques, Optical pumping with two finite linewidth lasers, *Phys. Rev. A* **41**, 4989 (1990).
- [52] B. Masterson, C. Tanner, H. Patrick, and C. Wieman, High-brightness, high-purity spin-polarized cesium beam, *Phys. Rev. A* **47**, 2139 (1993).
- [53] T. L. Gustavson, Ph.D. thesis, Stanford University (2000).
- [54] W. Demtröder, *Laser Spectroscopy 1: Basic Principles* (Springer, 2014).